International Journal of Minerals, Metallurgy and Materials
Volume 27, Number 8, August 2020, Page 1100
https://doi.org/10.1007/s12613-020-2094-0

Effect of microstructure and passive film on corrosion resistance of 2507 super duplex stainless steel prepared by different cooling methods in simulated marine environment

Min Zhu[1,2], *Qiang Zhang*[1], *Yong-feng Yuan*[1], *and Shao-yi Guo*[1]

1) School of Mechanical Engineering & Automation, Zhejiang Sci-Tech University, Hangzhou 310018, China
2) National and Local Joint Engineering Research Center of Reliability Analysis and Testing for Mechanical and Electrical Products, Zhejiang Sci-Tech University, Hangzhou 310018, China
(Received: 6 March 2020; revised: 24 April 2020; accepted: 11 May 2020)

Abstract: The effect of microstructure and passive film on the corrosion resistance of 2507 super duplex stainless steel (SDSS) in simulated marine environment was investigated by electrochemical measurements, periodic wet–dry cyclic corrosion test, scanning Kelvin probe force microscopy, atomic force microscopy, and X-ray photoelectron spectrometry. The results show that the occupation ratio of γ phase increases with the decrease in cooling rate, whereas the content of α phase reduces gradually. In addition, the σ precipitated phase only emerges in the annealed steel. The pitting sensitivity and corrosion rate of 2507 SDSS reduce first and then increase as the cooling rate decreases. The σ precipitated phase drastically reduces the protective ability of the passive film and facilitates micro-galvanic corrosion of the annealed steel. For various microstructures, the pits are preferentially distributed within the σ and γ phases. The corrosion resistance of 2507 SDSS prepared by different cooling methods is closely related to the microstructure and structure (stability and homogeneity) of the passive film. Normalized steel shows an optimal corrosion resistance, followed by the quenched and annealed steels.

Keywords: stainless steel; microstructure; corrosion resistance; passive film

1. Introduction

Metal corrosion must be encountered in the development of marine resources [1–4]. In general, the marine environment can be divided into five corrosion zones, such as ocean atmosphere, spray splash, tidal range, seawater immersion, and submarine soil zones. The spray splash area is typically the most corrosive area in marine environment, and this condition is ascribed to its characteristic wet–dry cyclic environment. On this account, the vulnerability to pitting corrosion of stainless steel used in this environment may be improved.

In recent years, increasing numbers of researchers have paid more attention to the corrosion behavior of metal materials in simulated wet–dry cyclic marine environments [5–11]. Thus far, the majority of studies on the corrosion of steel in marine environment are mainly focused on the different types of steel but less on the effect of microstructure on corrosion resistance [12–13]. Hao *et al*. [14] studied the stress corrosion cracking (SCC) mechanism of E690 high-strength steel under a simulated wet–dry cyclic marine environment and confirmed the high susceptibility of SCC in this environment. Yu *et al*. [15] investigated the corrosion behavior of X65 pipeline steel under periodic wet–dry cyclic and full immersion and observed pitting corrosion under a periodic wet–dry cyclic environment, whereas general corrosion occurred under full immersion area. The steel welded structure is ubiquitously applied in marine engineering. Corrosion occurs in such locations and is mainly derived from the complex microstructures of the welded joint area, such as nonhomogeneous microstructure, and different grain sizes. Similarly, the welded joints of stainless steel are susceptible to corrosion in marine environments. Unfortunately, no relevant literature reported the corrosion behavior of welded joints with different microstructures in wet–dry cyclic marine environments.

The 2507 super duplex stainless steel (SDSS), which is composed of austenite and ferrite phases, possesses a combination of outstanding properties, such as good mechanical properties, high temperature resistance, and high resistance to chloride stress corrosion cracking [16–18]. In the long run, SDSS will be increasingly applied in marine engineering and

Corresponding author: Min Zhu E-mail: zmii2009@163.com

offshore platforms owing to its beneficial properties [19–22]. Thereby, 2507 SDSS may suffer from wet–dry cyclic environment in the future service. Particularly, the environment may facilitate the corrosion of welded joints, causing heightened concerns about the use of stainless steel in marine environments. Lin *et al*. [23] studied the pitting corrosion behavior of SS304 stainless-steel welded joints in wet–dry cyclic environment and indicated that pitting nucleation and growth are promoted by the cycle. To date, limited research has been conducted on the corrosion behavior of simulated welded joints of 2507 SDSS in a wet–dry cyclic marine environment. Thus, the corrosion property of 2507 SDSS with different microstructures under periodic wet–dry cyclic marine environment must be investigated.

In this paper, the corrosion mechanisms of 2507 SDSS with various microstructures will be clarified from micro-galvanic corrosion caused by Volta potential differences together with the composition and structures of passive films. For these investigations, we focus on exhibiting the corrosion behavior of 2507 SDSS prepared by different cooling methods in a marine environment by employing several electrochemical measurements, periodic wet–dry cyclic corrosion test, atomic force microscopy (AFM), scanning Kelvin probe force microscopy (SKPFM), and X-ray photoelectron spectroscopy (XPS).

2. Experimental

2.1. Sample preparation and solution

The material studied in this paper was based on commercial SAF2507 SDSS (UNS S32750) with the following chemical composition (wt%): C 0.022, Si 0.55, Mn 0.69, Cr 25.15, Mo 3.43, Ni 6.74, P 0.029, Cu 0.13, S 0.002, N 0.27, and Fe balance. The heat treatment process was performed as follows. The samples were subjected to heating at 1060°C for 40 min, followed by water cooling, air cooling, or furnace cooling and named quenched, normalized, or annealed steels, respectively. The specimens obtained from heat treatment were used to simulate the microstructures within the welded joint area. The samples used in the electrochemical measurement and weight-loss test were sealed with epoxy resin, leaving a surface with 15 mm × 15 mm dimensions. All the samples were sequentially grinded to 2000 grit by SiC paper, cleaned with deionizer water and alcohol, and dried in air.

Afterward, the sample was chemically etched in 80 mL deionizer water + 20 mL hydrochloric acid + 0.3 g sodium metosulfite solution for 10 s. The microstructures were characterized by scanning electron microscopy (SEM, JEOL, and JSM-5610LV) and stereomicroscopy, and the proportions of different phases were calculated. The chemical composition of each phase was analyzed by mean of energy dispersive spectroscopy (EDS) equipped in a SEM system. Each EDS value was the average obtained for multiple data sets. The tests below were performed at least thrice.

2.2. Periodic wet–dry cyclic test

Periodic wet–dry cyclic test was performed in 3.5wt% NaCl solution at 30°C. The main experimental parameters were as follows. Each wet–dry cycle lasted for 1 h and included soaking and drying times of 15 and 45 min, respectively. The solution used in the test was changed at least once a day. During the experiment, several samples were taken out for electrochemical testing after the cycle test of 6 h. The remaining samples were taken out for weight-loss measurement after 10 d. After removing the corrosion products by 10vol% nitric acid solution (10 mL HNO_3 and 90 mL distilled water), the corrosion rate was calculated, and the corrosion morphology and pit initiation sites were observed by SEM.

2.3. Electrochemical tests

The electrochemical test was performed via CHI660 electrochemical workstation by using the traditional three-electrode system. The sample embedded in epoxy resin was selected as the working electrode, the platinum plate as counter electrode, and a saturated calomel electrode (SCE) as reference electrode. The electrolyte was 3.5wt% NaCl solution at 30°C to simulate the marine environment.

Electrochemical tests of the samples taken out in the periodic wet–dry cyclic chamber were performed as follows. First, the electrochemical impedance spectroscopy (EIS) test was conducted after testing the open-circuit potential (OCP) for 30 min. The test frequency ranged from 100 kHz to 10 mHz with an applied 10 mV signal amplitude. The impedance spectrum data were analyzed by ZSimpWin software. Subsequently, the polarization curve within a potential range of −1.2 V vs. SCE to 1.2 V vs. SCE was recorded at a scanning rate of 0.5 mV/s.

2.4. Electrochemical measurement of passive film after alternating current (AC) interference

AC interference is frequently detected in offshore marine engineering and seashore areas near super-high voltage transmission lines, which may promote the corrosion of 2507 SDSS employed in this region [24–26]. Hence, in this work, the corrosion resistance of passive film corresponding to various microstructures was evaluated by applying an AC current.

All the samples were successively grinded, polished, and cleaned to investigate the difference in corrosion susceptibility of the passive films formed by different microstructures. Then, the specimens were immersed continuously in 3.5wt% NaCl solutions at 30°C for 84 h. Afterward, the samples covered with passive film were subjected to the interference by AC current density of 50 $A \cdot m^{-2}$ for 4 min. Subsequently, EIS and Mott–Schottky tests were conducted after achieving

an approximately steady-state in the OCP test.

The parameters of EIS test are in accord with the above setting. The Mott–Schottky curve was recorded within a scanning potential range of −1 V vs. SCE to 0.9 V vs. SCE with 50 mV/steps at a frequency of 1 kHz.

2.5. *In situ* AFM measurement

The surface topography of passive film formed on different samples under AC interference was examined by an atomic force microscope (PSLA XE-100E AFM) using the non-contact mode. Prior to the experiment, all the samples were polished with 0.1 μm diamond powder immersed in 3.5wt% NaCl solutions for 84 h and interfered by superimposed AC for 4 min.

2.6. Magnetic microscopy (MFM) and SKPFM measurement

MFM and SKPFM tests based on AFM were performed on a dimension Nanoscope V (BRUKER Multimode 8) with multiple optional multimode SPM scan. The Nanoprobe™-coated magnetic Co/Cr on the front side and reflective Co/Cr on the back side were used as probes in MFM and SKPFM measurements, respectively. The probe material used was 0.01–0.025 Ω·cm antimony (n)-doped Si MESP model with a force constant of 1–5 $N \cdot m^{-1}$ and a resonant frequency of 60–100 kHz. Additionally, all tests were carried out at a constant temperature of 25°C. Regardless of MFM or SKPFM measurements, the surface morphologies of different samples were obtained in the first scan with the tapping mode at a scan rate of 0.996 Hz. In the second scan, the cantilever was lifted up to 100 nm to prevent the effect of topographic features.

2.7. Analysis of passive film composition

The chemical composition of the passive films formed on 2507 SDSS with various microstructures was investigated by the XPS. Prior to XPS measurement, the specimens with different microstructures were immersed continuously in 3.5wt% NaCl solution at 30°C for 84 h. Then, the samples covered with stable passive film was transferred to the XPS equipment after cleaning with deionizer water and dried in air. XPS analyses were performed using a monochromatic X-ray Al Kα source (Thermo Fisher Scientific, USA). The commercial software Xpspeak version 4.1 with a Shirley background subtraction was performed to fit the XPS data. The standard C 1s peak (284.8 eV) was used as the calibration peak.

3. Results and discussion

3.1. Microstructure and chemical composition

Fig. 1 shows the microstructures of 2507 SDSS prepared by different cooling methods. The normalized and quenched steels are composed of ferrite (α) and austenite phase (γ) without white σ precipitated phase, respectively (Fig. 1). Several α phases are embedded in the γ phase. However, the annealed steel contains not only α and γ phases but also numerous σ precipitated phases. The σ phase with irregular rod-shaped and granular structures are mainly distributed in the γ, α, and the boundaries of the two phases. With the drop in cooling rate, the volume fraction of γ phase increases, whereas that of α phase decreases.

Table 1 lists the concentrations of the major alloying elements in different phases of 2507 samples prepared by differ-

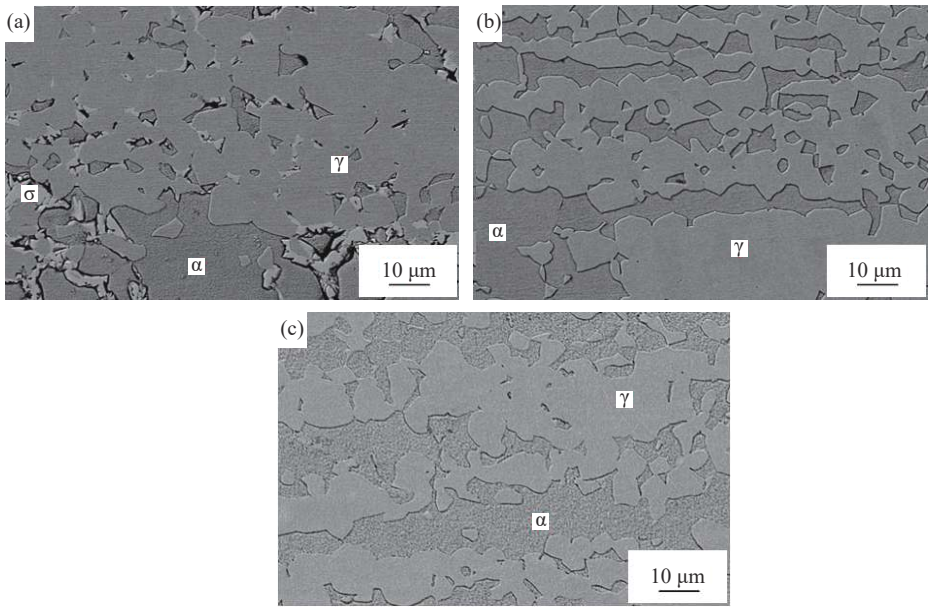

Fig. 1. Microstructure of 2507 SDSS prepared by different cooling methods: (a) annealed; (b) normalized; (c) quenched.

Table 1. Average chemical composition of alloying elements in different phases obtained by EDS and the calculative pitting resistance equivalent number (PREN) values

Cooling method	Phase	Chemical composition / wt%					PREN
		Cr	Mn	Ni	Mo	N	
Annealed	σ	27.00	1.13	3.25	8.65	—	—
	α	23.49	1.02	3.68	6.71	0.03	46.113
	γ	21.58	0.99	6.51	3.62	0.51	41.686
Normalized	α	24.54	0.89	4.06	6.21	0.05	45.833
	γ	21.95	1.07	6.29	3.81	0.48	42.203
Quenched	α	23.54	1.14	3.51	5.72	0.07	43.536
	γ	20.42	1.23	6.25	3.26	0.55	39.978

Note: PREN = $100w_{Cr} + 3.3 \times 100w_{Mo} + 16 \times 100w_{N}$, where w_i means the mass content of the i element in the phase of 2507 SDSS.

ent cooling methods. The α and γ phases within the normalized steel have more Cr and Mo compared with the quenched steel. The values of all the samples in Table 1 also indicate that more Cr and Mo are concentrated in the α phase, whereas the γ phase contains more Ni and Mn. Furthermore, the Cr and Mo contents in the σ precipitated phase are higher than those in the α and γ phases.

Fig. 2 depicts the effect of various cooling methods on the variations of phase fraction. The volume fraction of γ phase increases with the decrease in the cooling rate, whereas the volume fraction of α phase reduced gradually. In addition, the σ phase emerges in the annealed steel.

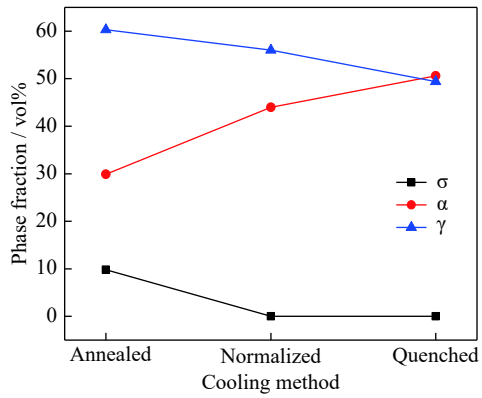

Fig. 2. Phase fraction of 2507 SDSS prepared by different cooling methods.

3.2. Electrochemical measurements under periodic wet–dry cyclic condition

Fig. 3 presents the evolution of OCP of various samples under a periodic wet–dry cyclic environment for 6 h in 3.5wt% NaCl solution at 30°C. The OCP values increases first and subsequently declined with the drop in cooling rate. The corrosion potential of the annealed sample is the most negative and eventually stabilizes at about −0.38 V, whereas the normalized sample shows a higher value compared with the quenched sample. The OCP can reflect the corrosion tendency. The lowest OCP indicates that the electrochemical activity of annealed steel is the highest. Thereby, the annealed sample has the highest corrosion tendency, followed by the quenched sample. Finally, the normalized sample corresponded to the minimum corrosion tendency.

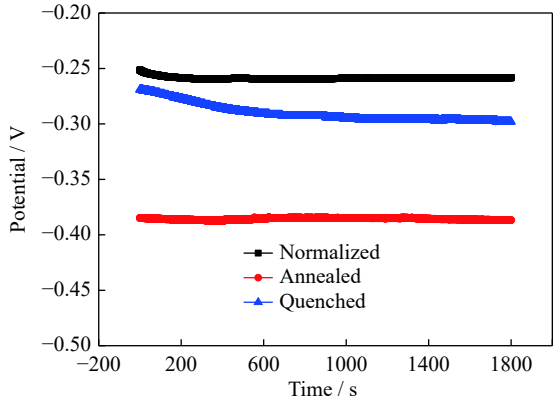

Fig. 3. OCP of 2507 SDSS prepared by different cooling methods under periodic wet–dry cyclic environment for 6 h.

Fig. 4 displays the electrochemical impedance spectra of various samples tested in a periodic wet–dry cyclic environment for 6 h. Regarding the Nyquist plots, all the capacitive reactance arcs display an incomplete semicircle, illustrating that the corrosion mechanism of 2507 SDSS prepared by different cooling methods is not modified. Evidently, the minimum diameter of capacitive loop is observed in the annealed steel, followed by that of quenched steel (Fig. 4(a)). In general, the large diameter of capacitive loop corresponds to a desirable anti-corrosion property [27–29]. This finding indicates that the annealed sample possesses the poorest corrosion resistance. According to the Bode plot in Fig. 4(b), the maximum impedence value (|Z|) of normalized steel within low frequency region corresponded to excellent corrosion resistance. In the spectra, Z_{re} and Z_{im} present the real and imaginary parts of the impedance, and f is frequency.

The equivalent circuit shown in Fig. 5 was used to fit the impedance spectrum data. In this model, R_s denotes the electrolyte resistance, Q_f represents the passive film capacitance, and R_f is the passive film resistance. Q_{dl} and R_{ct} denote the double–layer capacitance and charge transfer resistance, respectively [30–31]. The high-frequency region is closely re-

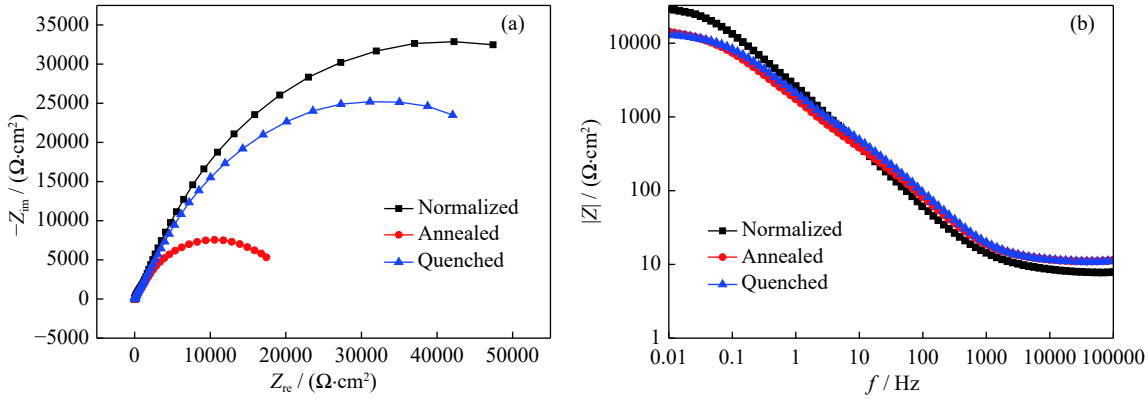

Fig. 4. Impedance spectra of 2507 SDSS prepared by different cooling methods under a periodic wet–dry cyclic environment for 6 h: (a) Nyquist plot; (b) Bode diagram.

lated to the corrosion resistance of the passive film, and the low-frequency area may be associated with charge transfer resistance. Table 2 shows the fitted results using the mentioned equivalent circuit. R_{ct} and R_f increase first and thereafter decrease accompanied by the decrease in cooling rate. On the other hand, the normalized steel exhibits the maximum R_f, which indicates that the steel has optimum stability and the protection of passive films. The maximum R_{ct} of the normalized steel shows no significant difference compared with that reported in literature [32], suggesting that the charge transfer process became harder. On the contrary, both R_f and R_{ct} of the annealed steel exhibit the minimum value. Hence, under the simulated wet–dry cyclic environment, the normalized steel shows the highest anti-corrosion property, followed by quenched and annealed steels.

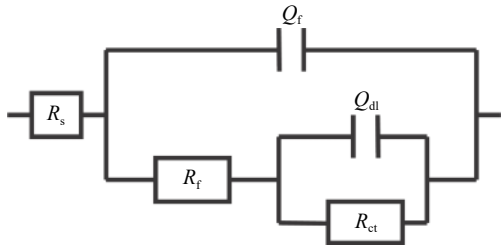

Fig. 5. Equivalent circuit for fitting EIS diagram.

Table 2. Fitted electrochemical parameters for EIS data of 2507 SDSS prepared with different cooling methods under periodic wet–dry cyclic environment for 6 h

Cooling method	R_s / (Ω·cm²)	Q_f / (10^{-5} F·cm^{-2})	n_f	R_f / (Ω·cm²)	Q_{dl} / (10^{-5} F·cm^{-2})	n_{dl}	R_{ct} / (10^4 Ω·cm²)
Annealed	44.81	2.084	0.8338	1527	2.666	0.8420	2.006
Normalized	28.00	2.240	0.8682	3876	2.442	0.8613	9.276
Quenched	22.06	2.809	0.8642	3810	3.629	0.8334	7.218

Note: n_f and n_{dl} are phenomenological coefficients.

Fig. 6 shows the potentiodynamic polarization curves E (potential)–i (current density) of various samples tested in a periodic wet–dry cyclic environment for 6 h. The evident passivation behavior of anodic polarization curves is observed, and this finding may be associated with the passive film that spontaneously formed on the samples under periodic wet–dry cyclic environment. In addition, the annealed steel possesses the narrowest passive region. Based on the analysis of polarization curves, the passive current density (i_p), critical pitting potential (E_p), and corrosion potential (E_{corr}) can be obtained (Table 3). Notably, the tendency of E_p first increases and subsequently decreases with the decrease in cooling rate. The E_p of normalized steel is slightly higher than that of quenched steel, whereas the annealed steel exhibits the lowest value. This finding reflects the lowest pitting susceptibility of normalized steel, that is, the passive film formed on the surface of normalized steel has the highest stability. Conversely, the annealed steel shows the highest pitting susceptibility compared with the other structure samples. Moreover, a small i_p corresponds to the low corrosion rate [33]. As a consequence, the lowest E_p and the highest i_p mean that the annealed steel possesses the poorest corrosion resistance. In the work of Zhang *et al.* [32], the difference between E_p and E_{corr} was applied to assess the passivity of steel. In general, the lower the E_p–E_{corr} value, the more inferior the pitting resistance of stainless steel is. The minimum E_p–E_{corr} value means that the annealed steel has a high pitting susceptibility under a periodic wet–dry cyclic environment (Table 3). The corrosion susceptibility of 2507 SDSS prepared by different cooling methods under a periodic wet–dry cyclic environment confirmed the results of EIS test.

Fig. 7 reveals the corrosion rate of 2507 SDSS prepared by different cooling methods under a periodic wet–dry cyclic environment for 10 d. The annealed steel exhibited the

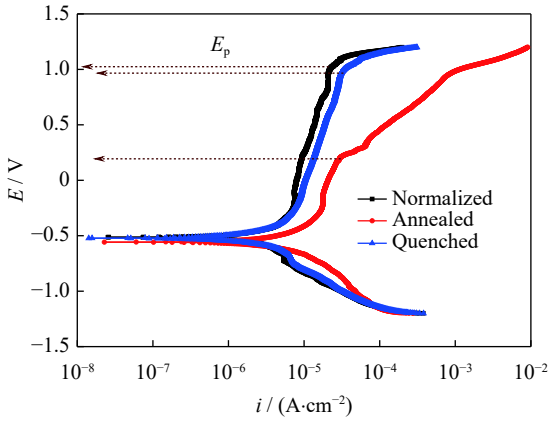

Fig. 6. Potentiodynamic polarization curve of 2507 SDSS prepared by different cooling methods under periodic wet–dry cyclic environment for 6 h.

Table 3. Electrochemical parameters for polarization curve of 2507 SDSS prepared by different cooling methods under periodic wet–dry cyclic environment for 6 h

Cooling method	i_p / (10^{-5} A·cm^{-2})	E_{corr} / V	E_p / V	(E_p−E_{corr}) / V
Annealed	2.10	−0.56	0.19	0.75
Normalized	0.90	−0.51	1.03	1.54
Quenched	1.28	−0.52	0.97	1.49

highest corrosion rate, followed by quenched and normalized steels.

Fig. 8 displays the corrosion morphology of 2507 SDSS prepared by different cooling methods under periodic wet–dry cyclic environment for 10 d. As revealed in Fig. 8(a), the annealed steel shows the most serious corrosion degree, with a large number of bright white pitting corrosion

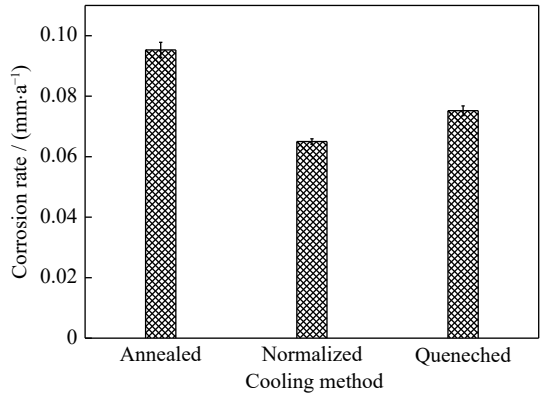

Fig. 7. Corrosion rate of 2507 SDSS prepared by different cooling methods under periodic wet–dry cyclic environment for 10 d.

and several small-sized pits connecting with each other to form the large-sized pits. The number of pits on the surface of quenched steel decreases to a certain extent compared with that of annealed steel. However, the observation of pit morphology indicates that the size and number of pits formed on normalized steel considerably reduce, implying a very slight corrosion degree. Therefore, the corrosion morphology reflects the difference in corrosion susceptibility of various microstructures.

The distribution of pitting corrosion is important to understand the corrosion susceptibility of different microstructures. Fig. 9 presents the pitting initiation sites of 2507 SDSS with different microstructures under periodic wet–dry cyclic environment for 10 d after removing the corrosion product. The annealed steel had the most severe corrosion degree, with a large number of pits located in the white precipitate phase (σ

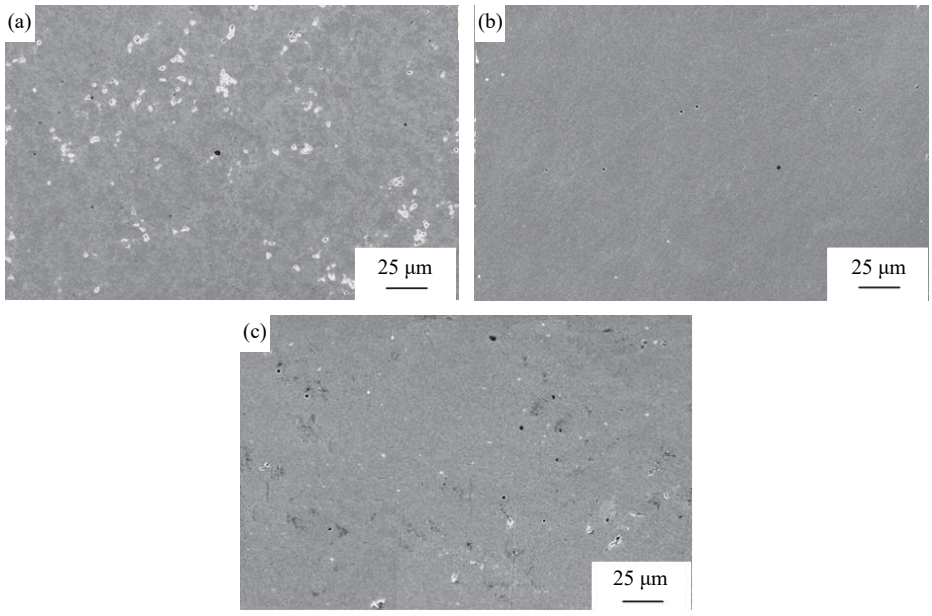

Fig. 8. Corrosion morphology of 2507 SDSS prepared by different cooling methods under periodic wet–dry cyclic environment for 10 d after removing the corrosion product: (a) annealed; (b) normalized; (c) quenched.

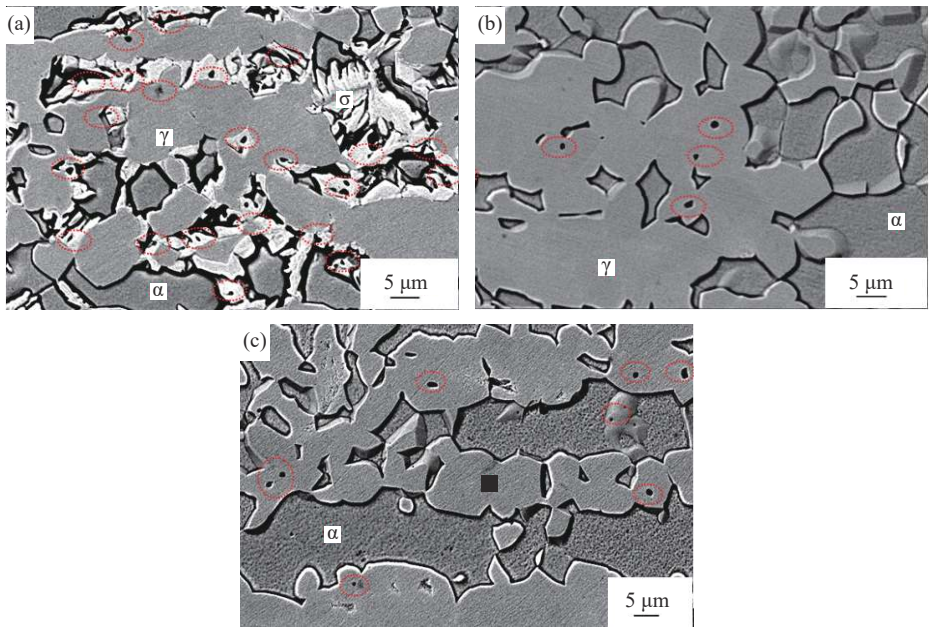

Fig. 9. Pitting position of 2507 SDSS under periodic wet–dry cyclic environment for 10 d after removing the corrosion product: (a) annealed; (b) normalized; (c) quenched.

phase) and several pits observed in the γ phase. These findings indicate that the σ precipitate phase within the annealed steel reduced the corrosion resistance of the steel. The EDS analysis showed that the γ phase contained less corrosion-resistant elements, such as Cr and Mo, than the α phase due to the precipitation of the σ phase. This finding can further account for the pitting corrosion distributed in the γ phase (Fig. 9(a)). As shown in Fig. 9(b), the normalized steel exhibited the minimum pits and the slightest corrosion degree in comparison with the other two samples. The pits mainly appeared in the γ phase, and several corrosion pits occurred in α the phase embedded within the γ phase. Similarly, Fig. 9(c) reveals that the majority of pits in the quenched steel were preferentially initiated in the γ phase, and a small number of pits occurred in the boundary areas of the α/γ phase. These results demonstrate the inseparable relationship between the microstructure and corrosion susceptibility of 2507 SDSS.

In periodic wet–dry cyclic environments, the results of the above tests suggest that the difference in corrosion resistance of steel is most likely to be related with its microstructures. The order of decreased corrosion resistance of 2507 SDSS with different microstructures was normalized steel, quenched steel, and annealed steel.

3.3. Passive film property test

The surface passive film significantly affects the corrosion susceptibility of stainless steel. According to the result of polarization curve and the value of R_f in Table 2, the passive films formed on various microstructures has different corrosion resistances. Therefore, to further reflect the difference among the three samples, we subjected the films formed on the samples to an interference with an AC current density of 50 $A \cdot m^{-2}$ for 4 min after immersion in 3.5wt% NaCl solution for 84 h. Then, electrochemical tests were performed, and the film morphology was analyzed by AFM measurement.

Fig. 10 displays the electrochemical impedance spectra of 2507 SDSS with different microstructures under AC interference. All curves in the Nyquist plots show the characteristics of semi-circle arcs with different diameters, whereas the diameter of capacitive loop of different samples first increases and then decreases with the increase in cooling rate. The Bode diagram is shown in Fig. 10(b). The minimum $|Z|$ value of annealed steel at the low-frequency region means that the passive film possessed the poorest corrosion resistance.

The equivalent circuit used for fitting the impedance spectra data is in agreement with the result shown in Fig. 5. Fig. 11 presents the variation of the fitted R_{ct} (charge transfer resistance) and R_f (passive film resistance) of different samples under AC interference. A substantial reduction in R_f is observed on the annealed steel, which suggests that the integrity and compactness of passive film interfered by AC interference are the poorest, leading to the easy penetration of the substrate surface by ions and molecules in the solution and accelerated electrode reaction. Moreover, the R_f and R_{ct} of the quenched specimen are slightly lower than those of normalized specimen. These results suggest that AC generates different damage impacts on the passive films formed on various microstructures. In consequence, the passive film formed on normalized steel possesses the greatest anti-corrosion property compared with the other steels.

Studying the properties of semiconductor passive film can explain the essential reasons for the corrosion resistance of

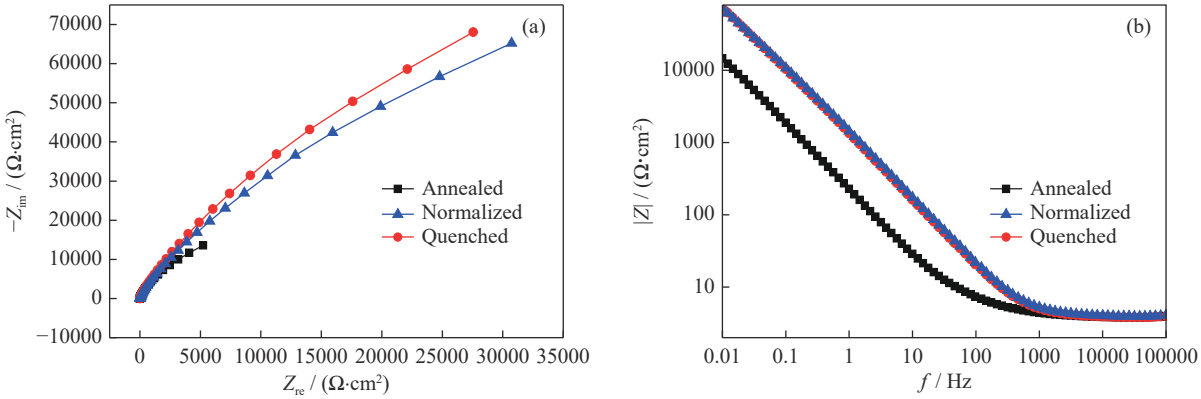

Fig. 10. Impedance spectra of 2507 SDSS prepared by different cooling methods under the interference with AC current density of i_{AC} = 50 A·m^{-2} for 4 min: (a) Nyquist plots; (b) Bode plots.

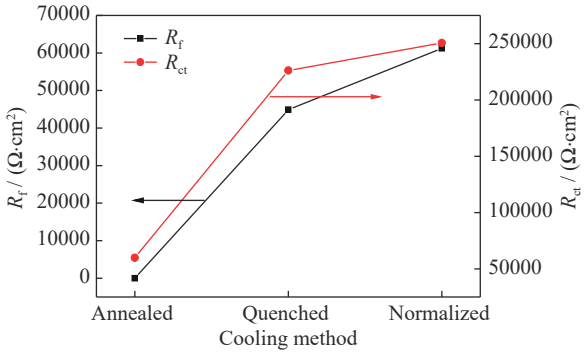

Fig. 11. R_{ct} and R_f of different samples under AC current interference.

passive films with different microstructures. Thereby, after AC interference, the semiconductor properties of passive films formed on 2507 SDSS with different microstructures were investigated by capacitance measurement [34–36]. The relationship between space charge capacitance (C) and applied potential can be given by the Mott–Schottky equations (1) and (2).

$$\frac{1}{C^2} = \frac{2}{\varepsilon\varepsilon_0 e N_D}\left(E - E_{fb} - \frac{kT}{e}\right), \text{ for n-type semiconductors} \quad (1)$$

$$\frac{1}{C^2} = -\frac{2}{\varepsilon\varepsilon_0 e N_A}\left(E - E_{fb} - \frac{kT}{e}\right), \text{ for p-type semiconductors} \quad (2)$$

where N_D and N_A are the donor and acceptor densities (cm^{-3}), respectively, e is the electron charge (1.602189 × 10^{-19} C), ε is the relative dielectric constant of the passive film, ε_0 is the permittivity of the vacuum (8.854 × 10^{-12} F·m^{-1}), T is the Kelvin temperature, k is Boltzmann's constant (1.38 × 10^{-23} J·K^{-1}), E is the applied electrode potential (V vs. SCE), and E_{fb} is the flat band potential (V vs. SCE). N_D and N_A can be calculated from the slopes of the linear portion of Mott–Schottky curves.

Fig. 12 presents the Mott–Schottky plots of 2507 SDSS with various microstructures under the interference of AC current. All three curves show an inflection point around −0.4 V, which implies the change in electronic properties. The capacitive test displays the presence of two linear regions in all plots, and the positive slope indicates that the passive film presents an n-type semiconductor behavior. Conversely, a negative slope suggests the p-type semiconductor. Hence, the surface passive film of different microstructures reveals the characteristics of p-n type semiconductors. As revealed in Table 4, the annealed steel displays the highest N_D and N_A, followed by the quenched steel, whereas the normalized steel exhibits the minimum value. The higher the number of carrier density, the more defects contained within the passive film. The defect makes the passive film prone to rupture, causing the pitting corrosion to preferentially initiate at the damage site in the passive film.

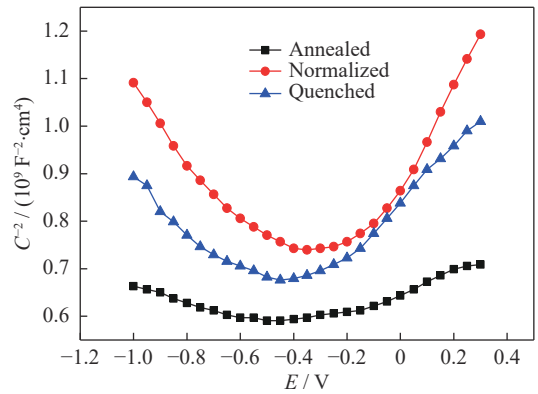

Fig. 12. Mott–Schottky plots of 2507 SDSS with various microstructures under interference with AC current density i_{AC} = 50 A·m^{-2} for 4 min.

Under AC interference, the maximum carrier density value indicates that the stability and protection of the passive film formed on the surface of annealed steel are the lowest compared with those of the other steels. The film on normalized steel has optimal stability and protection. Thereby, the

Table 4. Calculated donor and acceptor densities of passive films of 2507 SDSS with various microstructures under AC interference (i_{AC} = 50 A·m^{-2}) for 4 min

Cooling method	N_D / (10^{20} cm^{-3})	N_A / (10^{20} cm^{-3})
Annealed	23.51	18.81
Normalized	6.7167	5.531
Quenched	10.448	7.233

corrosion behavior of 2507 SDSS with different microstructures is affected by the structure of the passive film to a certain extent.

Fig. 13 exhibits the AFM morphology of surface passive films of samples prepared by different cooling methods. The findings reflect the integrity of passive films formed on the samples with different microstructures after AC interference. Cellular and granular structures are observed on the surface passive film. The passive film on the surface of annealed steel contains numerous defects characterized by holes in the dark area (circled section in Fig. 13(a)). These defects provide channels for the entry of harmful ions, and pitting corrosion preferentially occurs at the damaged region within the film (Fig. 9(a)). Meanwhile, the corrosion morphology in Fig. 8(a) proves that the annealed steel has the severest corrosion degree, containing a considerable number of pits. As shown in Fig. 13(c), the number of film defects formed on the quenched steel are remarkably reduced. Compared with normalized steel (Fig. 13(b)), the uneven film morphological characteristics, such as the difference in particle size and height, may be conducive to the concentration of harmful ions in the solution, resulting in film breakdown and accelerated pitting. By contrast, the surface film of the normalized steel with AC application is relatively homogeneous and flat.

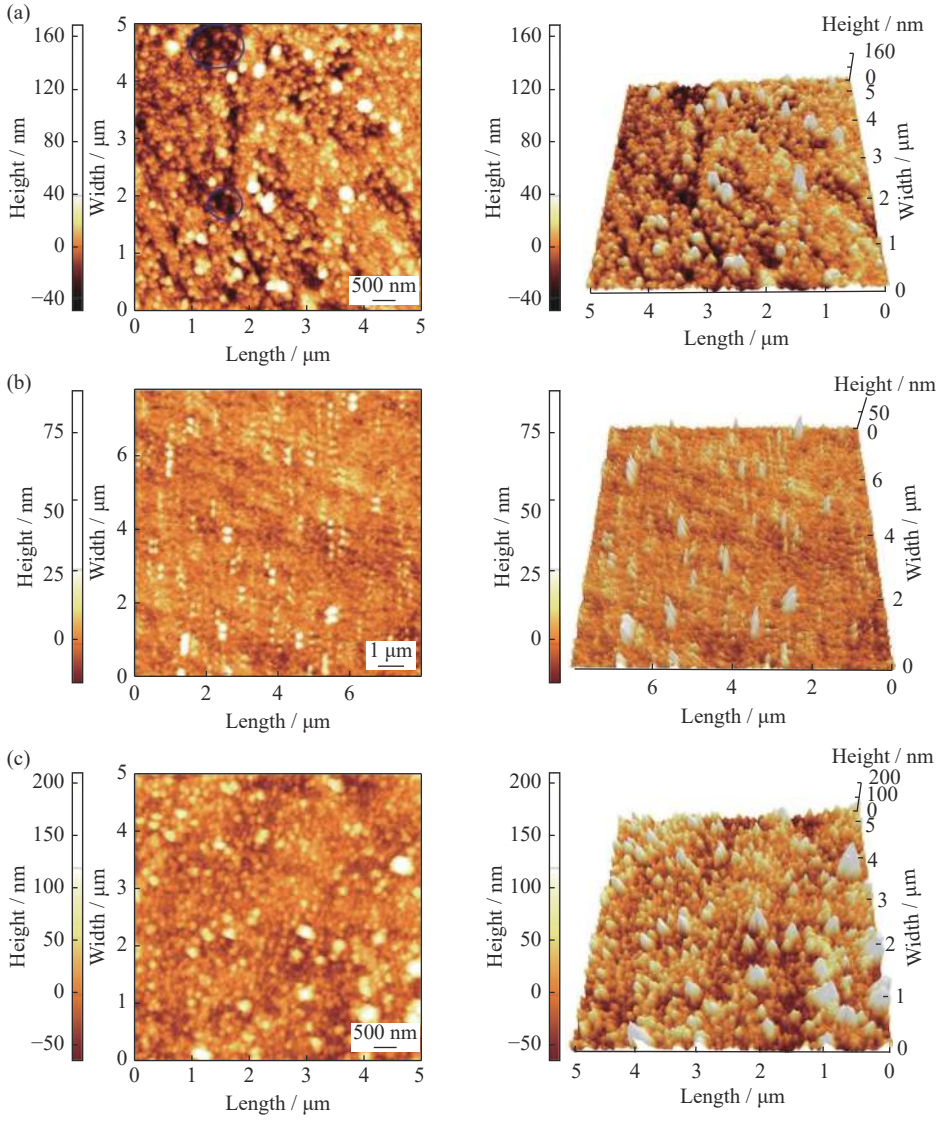

Fig. 13. 2D AFM images and the corresponding 3D morphologies of passive films on 2507 SDSS prepared by different cooling methods under the interference of AC current density (i_{AC} = 50 A·m^{-2}) for 4 min: (a) annealed; (b) normalized; (c) quenched.

This morphological characteristic considerably improves the stability and protection of the film.

In summary, the results acquired from EIS test, Mott–Schottky curve, and AFM measurement demonstrate that the passive films formed on different microstructures showed varied uniformity, stability, and protection under the same AC interference. Therefore, the difference in corrosion susceptibility of 2507 SDSS may be directly attributed to the passive film formed on various microstructures.

3.4. Volta potential analysis

Fig. 14 shows the MFM and SKPFM diagrams of the three samples with different microstructures. As shown in Figs. 14(b_1)–14(b_3), the SKPFM images correspond to the same area of MFM images (Figs. 14(a_1)–14(a_3). Figs. 14(c_1)–14(c_3) depict the Volta potential difference variation of straight lines passing through different phases in the SKPFM images. The phases within different microstructures in Volta potential maps can be distinguished by observing the morphological characteristics of SEM and MFM images. According to the obtained results, the Volta potential of ferrite phase (α) is considerably lower than that of austenite phase (γ) in all samples, which agree with the findings of previous studies [37–39]. For normalized and quenched steels, the maximum Volta potential difference at interfaces between the α and γ phases are approximately 63 and 70 mV, respectively, which are calculated by the subtract between the nobler γ potential and the low α potential, as marked in the red circles. The great Volta potential difference between the α and γ phases in the quenched steel represents the large driving force to generate micro-galvanic corrosion. Thus, the corrosion resistance of quenched steel is slightly lower than that of normalized steel. For the annealed steel, as shown in Fig. 14(c_1), the marked high austenite Volta potential and low ferrite potential in annealed steel are 13 and −26 mV, respectively. The σ precipitated phase possesses the highest Volta potential of 24 mV compared with those of ferrite and austenite phases in annealed steel. Thus, the probability of micro-galvanic corrosion is vastly enhanced due to the Volta potential differences between the α, γ, and σ phases. Given this result, the amount of micro-galvanic corrosion cells of this multiphase structure is well above that of other microstructures. Thus, its corrosion resistance is considerably reduced in spite of the relative low Volta potential difference. Moreover, the above electrochemical test and AFM results indicate that the passive films formed on different microstructures have varied corrosion resistances, which may be associated with various microstructures and uneven distribution of alloy elements [40–41]. Based on the above analysis results, the annealed steel possessed the poorest corrosion resistance.

According to Figs. 14(c_2) and 14(c_3), the Volta potential of austenite phase is nobler than that of ferrite phase in normalized and quenched steels. However, Figs. 9(b) and 9(c) reflect that the pits are mainly distributed in the austenite phase, whereas few pits emerge in the ferrite phase. The possible causes are listed below. Volta potential is only suitable for predicting the corrosion tendency and cannot reflect the actual kinetics [37,42]. The distribution law of pitting is explained by the value of PREN. In general, PREN can reflect the difference of pitting corrosion resistance between the α and γ phases [43–47]. A high PREN value means a high anti-localized corrosion capability. Combined with the element contents in EDS results and the calculated PREN values (Table 1), the anti-localized corrosion capability of ferrite phase is greater than that of austenite phase in all samples with different microstructures, suggesting that austenite phase, which acts as the anode in the micro-galvanic corrosion cells, is easily subject to pitting initiation. Thereby, pits preferentially emerge in the γ phase (Fig. 9).

Nevertheless, the pits formed on annealed steel are mainly distributed in the σ precipitated phase. The corrosion resistance of the σ phase cannot simply depend on the distribution of Cr, Mo, and other alloy elements. The structural characteristics of the phase and the formation of passive film should also be fully considered. On the one hand, according to the results of line scanning EDS (Fig. 15), the precipitation of σ phase causes a vast difference in the distribution of Cr, Mo, and other alloy elements among the α, γ, and σ phases, which will inevitably lead to the formation of uneven passive film on the surface of the steel substrate. Thus, the stability of the passive film vastly decreases. Additionally, the higher the element concentration gradient, the more apparent the difference of corrosion susceptibility of passive film is. Although the σ phase is rich in Cr, Mo, and other alloying elements, its structure differed from the surrounding matrix phases of γ and α, which would also degrade the stability of the passive film formed on the σ precipitated phase. The results of polarization curve, EIS test, and Mott–Schottky plots, especially the apparent decrease of E_p and the increase in i_p value, can prove this point. Furthermore, AFM morphology directly demonstrates that the presence of σ phase significantly declines the uniformity, stability, and protection of the passive film formed on the annealed steel. Fig. 9(a) shows that the σ precipitated phase can be viewed as the anode, and the other matrix phases composed of γ and α act as the cathode, resulting in a substantial micro-galvanic corrosion. The corrosion current density of the anode is highly attributed to the small area of the σ phase. Consequently, the corrosion of σ phase is accelerated due to the electrochemical corrosion effect between the small anode and large cathode, and the pits preferentially form within the σ precipitated phase. Thus, the σ phase drastically reduces the uniformity, stability, and protection of the surface passive film and promotes the pitting corrosion.

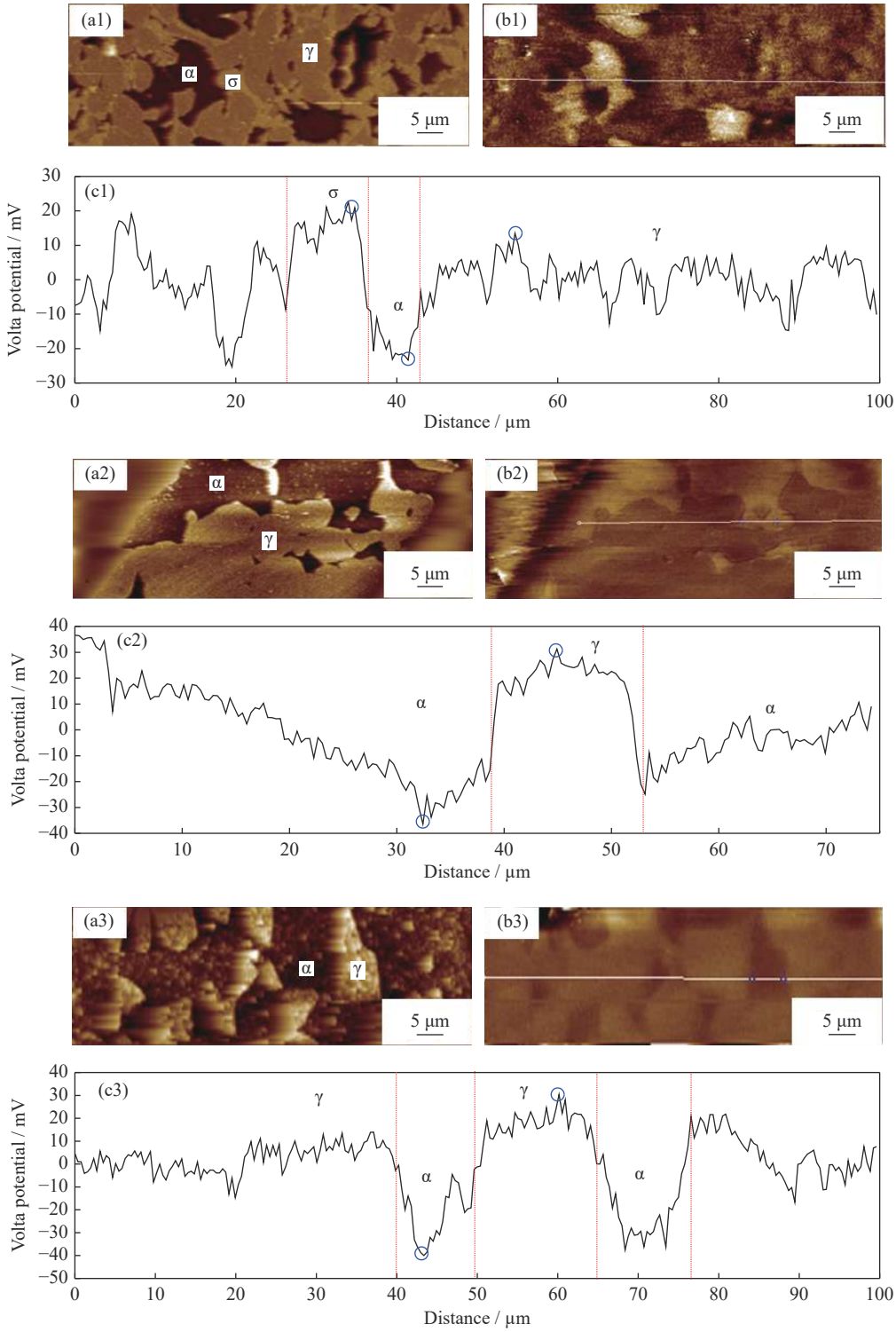

Fig. 14. MFM and SKPFM images of the annealed (a_1, b_1), normalized (a_2, b_2), and quenched (a_3, b_3) steels. (c_1–c_3) Volta potential difference profile of the line shown in b_1–b_3.

3.5. XPS studies

The corrosion resistance of 2507 SDSS with various microstructures is related to the composition of the passive film. Thus, the difference in its composition must be investigated via XPS measurement. Figs. 16–17 show the XPS peaks of the main elements (Fe 2p, Cr 2p, O 1s, and Mo 3d) in the passive film. Table. 5 lists the binding energies [48–49] obtained from XPS spectra deconvolution.

Figs. 16(a_1)–16(a_3) display the fitted spectra of Fe $2p_{3/2}$ of

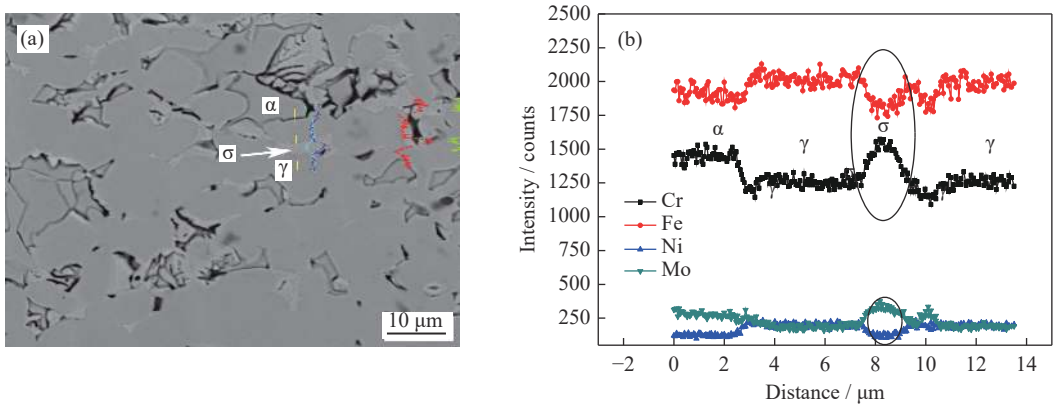

Fig. 15. SEM image (a) and element content variation (b) of different phases in annealed steel.

Table 5. Binding energy of the primary compounds of passive films formed on various microstructures

Element	Binding energy / eV
Cr	$Cr_{(met)}$/574.1; Cr_2O_3/576.3; $Cr(OH)_3$/577.1
Fe	$Fe_{(met)}$/706.7; Fe_3O_4/708.2; FeO/709.4; Fe_2O_3/710.9
O	O^{2-}/530; OH^- /531.5; H_2O/533
Mo	$Mo_{(met)}$/227.4; Mo^{4+}/230.2; Mo^{6+}/232.2
	$Mo_{(met)}$/230.9; Mo^{4+}/233.4; Mo^{6+}/235.1/235.1

the passive films formed on various microstructures, which split into four constituent peaks, corresponding to Fe, FeO, Fe_2O_3, and Fe_3O_4. The high intensities of Fe_2O_3 and FeO illustrate that Fe^{2+} and Fe^{3+} are the primary species of iron oxide in the passive film. The Cr $2p_{3/2}$ spectra shown in Figs. 16(b_1)–16(b_3) are the composition of three constituent peaks, which correspond to the formation of $Cr_{(met)}$, Cr_2O_3, and $Cr(OH)_3$, respectively. The Cr_2O_3 concentration of all samples is the highest, which indicates that the compound played an important role in the corrosion resistance of the passive film. The Mo 3d spectra are fitted by six peaks of Mo $3d_{3/2}$ and Mo $3d_{5/2}$ (Fig. 17(b_1)–17(b_3)). As for the Mo 3d species formed on annealed steel, the intensity of Mo^{4+} is the highest. For the quenched and normalized steels, however,

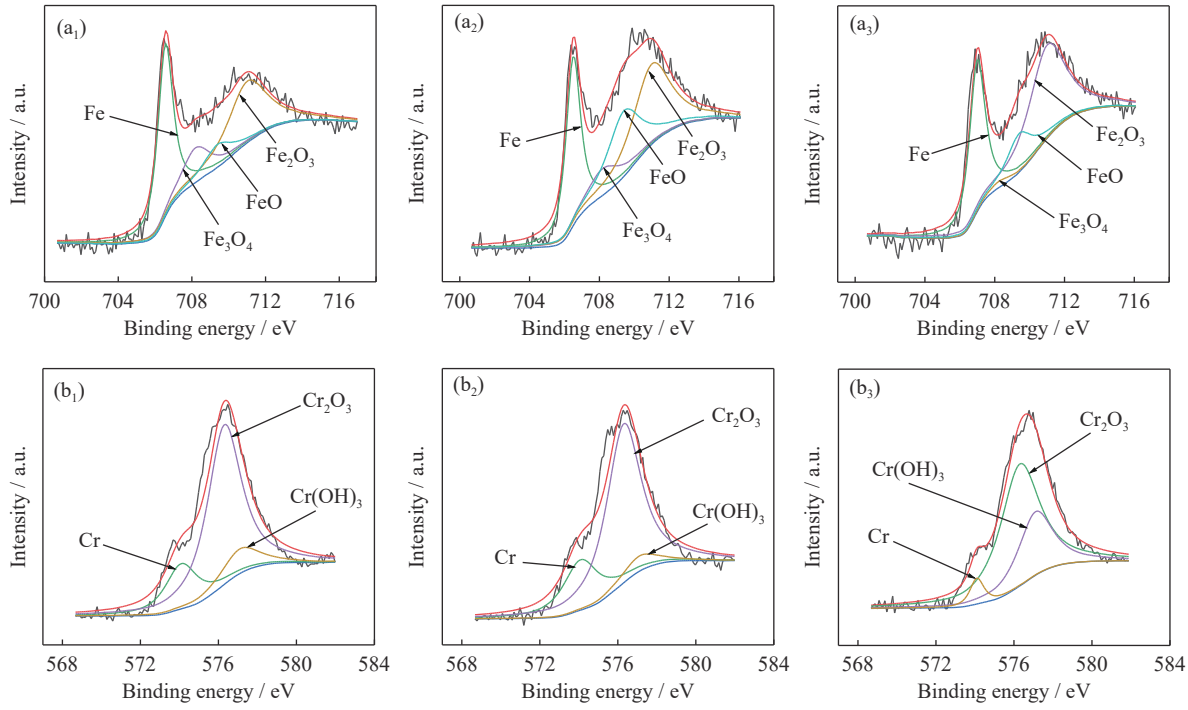

Fig. 16. XPS spectra of Fe $2p_{3/2}$ and Cr $2p_{3/2}$ of the passive films formed on annealed (a_1, b_1), quenched (a_2, b_2), and normalized steels (a_3, b_3).

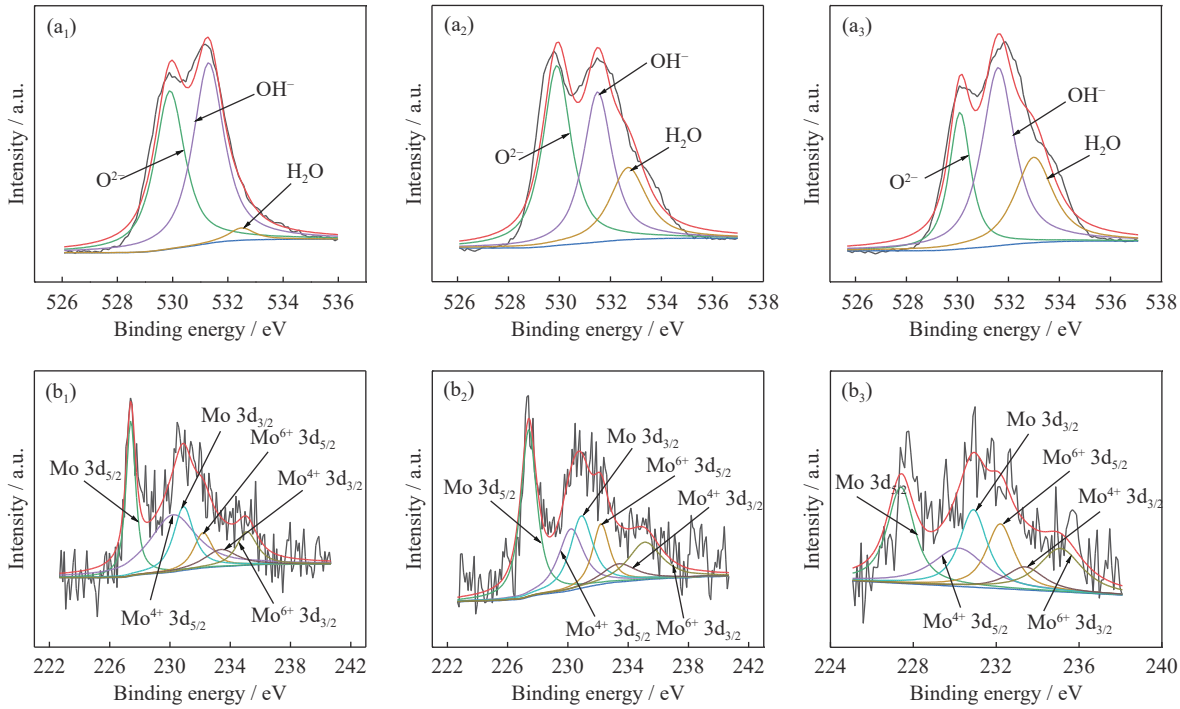

Fig. 17. XPS spectra of O 1s and Mo 3d of the passive films formed on annealed (a_1, b_1), quenched (a_2, b_2), and normalized steels (a_3, b_3).

Mo^{6+} is the primary constituent of the passive film. In general, the appearance of Mo^{6+} is more effective than that of other passive species, enhancing the stability of passive film [50–51]. Therefore, the passive film on the surface of annealed steel has the poorest stability. According to the results of the fitted spectra of O 1s in Figs. 17(a_1)–17(a_3), the three distinct peaks assigned to O^{2-}, OH^-, and H_2O can be observed. The relatively high intensities of O^{2-} and OH^- in the three samples correspond to the formation of oxide and hydroxide in the passive film. Furthermore, the concentration of bound water in annealed steel reduces compared with that of the other two samples. Hashimoto *et al.* [52] demonstrated that the bound water may degrade the nonuniformity of the passive film. Consequently, the stability and homogeneity of passive film formed on quenched steel and normalized steel significantly improve.

According to the above XPS results, a minimal difference is observed in the composition of passive films formed on various microstructures. Combined with the results of EIS, MS, and AFM tests under AC interference, we can infer that the structure of passive film (stability and homogeneity) largely affects the corrosion resistance of different microstructures compared with the composition of passive film.

4. Conclusions

The influence of microstructure and passive film on the corrosion behavior of 2507 SDSS was investigated, and the main conclusions can be summarized as follows.

(1) The occupation ratio of γ phase increased with the decrease in cooling rate, whereas the content of α phase reduced gradually. In addition, the σ precipitated phase only emerged in the annealed steel.

(2) Under periodic wet–dry cyclic environment, the normalized steel showed an optimal corrosion resistance, followed by the quenched steel and finally the annealed steel. For the annealed steel with a multiphase structure, the pits were mainly distributed in the σ precipitated phase, which is attributed to preferential dissolution of the σ phase as the anode during corrosion. The PREN value of α phase was larger than that of γ phase in all samples. Thus, the pits preferentially occurred in the γ phase.

(3) The electrochemical measurement results revealed that the passive films formed on various microstructures with AC application had different uniformity and stability. The AFM topographic morphology of passive film supplied a direct evidence for the corrosion resistance of 2507 SDSS with different microstructures. Moreover, the structure of passive film considerably affects the corrosion resistance of various microstructures.

(4) For the annealed steel, the σ phase considerably degraded the stability of the surface passive film and increased the amount of micro-galvanic corrosion cells. This finding may be ascribed to the multiphase structure, which accelerated the pitting corrosion. Compared with the normalized steel, the Volta potential difference between the α and γ phases was higher in the quenched steel, which represents the larger driving force of micro-galvanic corrosion, resulting in

the more severe corrosion degree in the quenched microstructure. However, the Volta potential of ferrite was lower than that of austenite phase, which reflects the corrosion tendency.

Acknowledgements

This work was financially supported by the National Natural Science Foundation of China (No. 51871026) and the Natural Science Foundation of Zhejiang Province, China (No. LY18E010004), and some experiment works were supported by the National Material Environmental Corrosion Infrastructure, China.

References

[1] X. Zhang, W.Z. Wei, L. Cheng, J. Liu, K.M. Wu, and M. Liu, Effects of niobium and rare earth elements on microstructure and initial marine corrosion behavior of low-alloy steels, *Appl. Surf. Sci.*, 475(2019), p. 83.

[2] H.C. Ma, Y. Fan, Z.Y. Liu, C.W. Du, and X.G. Li, Effect of pre-strain on the electrochemical and stress corrosion cracking behavior of E690 steel in simulated marine atmosphere, *Ocean Eng.*, 182(2019), p. 188.

[3] M. Cao, L. Liu, Z.F. Yu, L. Fan, and F.H. Wang, Electrochemical corrosion behavior of 2A02 Al alloy under an accelerated simulation marine atmospheric environment, *J. Mater. Sci. Technol.*, 35(2019), No. 4, p. 651.

[4] Z.Y. Liu, W.K. Hao, W. Wu, H. Luo, and X.G. Li, Fundamental investigation of stress corrosion cracking of E690 steel in simulated marine thin electrolyte layer, *Corros. Sci.*, 148(2019), p. 388.

[5] C.Q. Cheng, L.I. Klinkenberg, Y. Ise, J. Zhao, E. Tada, and A. Nishikata, Pitting corrosion of sensitised type 304 stainless steel under wet–dry cycling condition, *Corros. Sci.*, 118(2017), p. 217.

[6] N.W. Dai, Q.M. Chen, J.X. Zhang, X. Zhang, Q.Z. Ni, Y.M. Jiang, and J. Li, The corrosion behavior of steel exposed to a DC electric field in the simulated wet-dry cyclic environment, *Mater. Chem. Phys.*, 192(2017), p. 190.

[7] X. Zhang, S.W. Yang, W.H. Zhang, H. Guo, and X.L. He, Influence of outer rust layers on corrosion of carbon steel and weathering steel during wet-dry cycles, *Corros. Sci.*, 82(2014), p. 165.

[8] X.G. Li, D.W. Zhang, Z.Y. Liu, Z. Li, C.W. Du, and C.F. Dong, Materials science: Share corrosion data, *Nature*, 527(2015), No. 7579, p. 441.

[9] A.N. Chen, F.H. Cao, X.N. Liao, W.J. Liu, L.Y. Zheng, J.Q. Zhang, and C.A. Cao, Study of pitting corrosion on mild steel during wet–dry cycles by electrochemical noise analysis based on chaos theory, *Corros. Sci.*, 66(2013), p. 183.

[10] Z.F. Wang, F.X. Yin, L.X. Wu, Y.Q. Sun, and W.L. Zhang, Corrosion resistance on high strength bainitic steel and 09CuPCrNi after wet–dry cyclic conditions, *J. Iron Steel Res. Int.*, 20(2013), No. 2, p. 72.

[11] J.Q. Wu, B. Diao, W.M. Zhang, Y.H. Ye, Z.J. Liu, and D. Wang, Chloride diffusivity and service life prediction of fatigue damaged RC beams under seawater wet–dry environment, *Constr. Build. Mater.*, 171(2018), p. 942.

[12] W. Han, C. Pan, Z.Y. Wang, and G.C. Yu, A study on the initial corrosion behavior of carbon steel exposed to outdoor wet–dry cyclic condition, *Corros. Sci.*, 88(2014), p. 89.

[13] B. Qian, B.R. Hou, and M. Zheng, The inhibition effect of tannic acid on mild steel corrosion in seawater wet/dry cyclic conditions, *Corros. Sci.*, 72(2013), p. 1.

[14] W.K. Hao, Z.Y. Liu, W. Wu, X.G. Li, C.W. Du, and D.W. Zhang, Electrochemical characterization and stress corrosion cracking of E690 high strength steel in wet–dry cyclic marine environments, *Mater. Sci. Eng. A*, 710(2018), p. 318.

[15] J.X. Yu, H.K. Wang, Y. Yu, Z. Luo, W.D. Liu, and C.M. Wang, Corrosion behavior of X65 pipeline steel: Comparison of wet–dry cycle and full immersion, *Corros. Sci.*, 133(2018), p. 276.

[16] H.Y. Ha, M.H. Jang, T.H. Lee, and J. Moon, Understanding the relation between phase fraction and pitting corrosion resistance of UNS S32750 stainless steel, *Mater. Charact.*, 106(2015), p. 338.

[17] Z.Y. Zhang, H.Z. Zhang, J. Hu, X.X. Qi, Y. Bian, A. Shen, P.P. Xu, and Y.Q. Zhao, Microstructure evolution and mechanical properties of briefly heat-treated SAF 2507 super duplex stainless steel welds, *Constr. Build. Mater.*, 168(2018), p. 338.

[18] Y. Zhao, Y. Wang, S. Tang, W.N. Zhang, and Z.Y. Liu, Edge cracking prevention in 2507 super duplex stainless steel by twin-roll strip casting and its microstructure and properties, *J. Mater. Process. Technol.*, 266(2019), p. 246.

[19] Z.H. Sun, M. Moradi, Y.X. Chen, R. Bagheri, P.S. Guo, L.J. Yang, Z.L. Song, and C. Xu, Simulation of the marine environment using bioreactor for investigation of 2507 duplex stainless steel corrosion in the presence of marine isolated *Bacillus Vietnamensis* bacterium, *Mater. Chem. Phys.*, 208(2018), p. 149.

[20] Z.Y. Cui, S.S. Chen, Y.P. Dou, S.K. Han, L.W. Wang, C. Man, X. Wang, S.G. Chen, Y.F. Cheng, and X.G. Li, Passivation behavior and surface chemistry of 2507 super duplex stainless steel in artificial seawater: Influence of dissolved oxygen and pH, *Corros. Sci.*, 150(2019), p. 218.

[21] J.M. Pardal, S.S.M. Tavares, M.C. Fonseca, J.A. de Souza, R.R.A. Côrte, and H.F.G. de Abreu, Influence of the grain size on deleterious phase precipitation in superduplex stainless steel UNS S32750, *Mater. Charact.*, 60(2009), No. 3, p. 165.

[22] J.C.de Lacerda, L.C. Cândido, and L.B. Godefroid, Effect of volume fraction of phases and precipitates on the mechanical behavior of UNS S31803 duplex stainless steel, *Int. J. Fatigue*, 74(2015), p. 81.

[23] C. Lin, X.G. Li, and C.F. Dong, Pitting and galvanic corrosion behavior of stainless steel with weld in wet–dry environment containing Cl^-, *J. Univ. Sci. Technol. Beijing*, 14(2007), No. 6, p. 517.

[24] Q. Liu, W. Wu, Y. Pan, Z.Y. Liu, X.C. Zhou, and X.G. Li, Electrochemical mechanism of stress corrosion cracking of API X70 pipeline steel under different AC frequencies, *Constr. Build. Mater.*, 171(2018), p. 622.

[25] N.W. Dai, J. Wu, L.C. Zhang, Y.T. Sun, Y.Y. Liu, Y.Y. Yang, Y.M. Jiang, and J. Li, Alternating voltage induced oscillation on electrochemical behavior and pitting corrosion in duplex stainless steel 2205, *Mater. Corros.*, 70(2019), No. 3, p. 419.

[26] D.K. Kim, S.V. Muralidharan, T.H. Ha, J.H. Bae, Y.C. Ha, H.G. Lee, and J.D. Scantlebury, Electrochemical studies on the alternating current corrosion of mild steel under cathodic protection condition in marine environments, *Electrochim. Acta*, 51(2006), No. 25, p. 5259.

[27] M. Liu, X.Q. Cheng, X.G. Li, and T.J. Lu, Corrosion behavior of low-Cr steel rebars in alkaline solutions with different pH in

the presence of chlorides, *J. Electroanal. Chem.*, 803(2017), p. 40.
[28] J.L. Lv, W.L. Guo, and T.X. Liang, The effect of pre-deformation on corrosion resistance of the passive film formed on 2205 duplex stainless steel, *J. Alloys Compd.*, 686(2016), p. 176.
[29] M.Q. Wang, Z.H. Zhou, Q.J. Wang, Z.H. Wang, X. Zhang, and Y.Y. Liu, Role of passive film in dominating the electrochemical corrosion behavior of FeCrMoCBY amorphous coating, *J. Alloys Compd.*, 811(2019), art. No. 151962.
[30] A. Kocijan, D.K. Merl, and M. Jenko, The corrosion behaviour of austenitic and duplex stainless steels in artificial saliva with the addition of fluoride, *Corros. Sci.*, 53(2011), No. 2, p. 776.
[31] J. Ming and J.J. Shi, Chloride resistance of Cr-bearing alloy steels in carbonated concrete pore solutions, *Int. J. Miner. Metall. Mater.*, 27(2020), No. 4, p. 494.
[32] L.H. Zhang, W. Zhang, Y.M. Jiang, B. Deng, D.M. Sun, and J. Li, Influence of annealing treatment on the corrosion resistance of lean duplex stainless steel 2101, *Electrochim. Acta*, 54(2009), No. 23, p. 5387.
[33] L. Freire, M.J. Carmezima, M.G.S. Ferreira, and M.F. Montemor, The electrochemical behaviour of stainless steel AISI 304 in alkaline solutions with different pH in the presence of chlorides, *Electrochim. Acta*, 56(2011), No. 14, p. 5280.
[34] L. Zeng, X.P. Guo, G.A. Zhang, and H.X. Chen, Semiconductivities of passive films formed on stainless steel bend under erosion-corrosion conditions, *Corros. Sci.*, 144(2018), p. 258.
[35] S. Ningshen, U. Kamachi Mudali, V.K. Mittal, and H.S. Khatak, Semiconducting and passive film properties of nitrogen-containing type 316LN stainless steels, *Corros. Sci.*, 49(2007), No. 2, p. 481.
[36] M. Liu, Y.Q. Hao, L.R. Zheng, L. Niu, and D. Miao, Role of coke in the passive properties of vitallium 2000 CoCrMo casting alloy in simulated oral environment, *J. Mater. Eng. Perform.*, 28(2019), No. 12, p. 7527.
[37] Y.J. Guo, T.Y. Sun, J.C. Hu, Y.M. Jiang, L.Z. Jiang, and J. Li, Microstructure evolution and pitting corrosion resistance of the Gleeble-simulated heat-affected zone of a newly developed lean duplex stainless steel 2002, *J. Alloys Compd.*, 658(2016), p. 1031.
[38] L.Q. Guo, M. Li, X.L. Shi, Y. Yan, X.Y. Li, and L.J. Qiao, Effect of annealing temperature on the corrosion behavior of duplex stainless steel studied by *in situ* techniques, *Corros. Sci.*, 53(2011), No. 11, p. 3733.
[39] N. Sathirachinda, R. Pettersson, and J.S. Pan, Depletion effects at phase boundaries in 2205 duplex stainless steel characterized with SKPFM and TEM/EDS, *Corros. Sci.*, 51(2009), No. 8, p. 1850.
[40] Z.Q. Zhang, H.Y. Jing, L.Y. Xu, Y.D. Han, L. Zhao, and J.L. Zhang, Influence of microstructure and elemental partitioning on pitting corrosion resistance of duplex stainless steel welding joints, *Appl. Surf. Sci.*, 394(2017), p. 297.
[41] Q. Sun, J. Wang, H.B. Li, Y. Li, Y.D. Hu, J.G. Bai, and P.D. Han, Chi phase after short-term aging and corrosion behavior in 2205 duplex stainless steel, *J. Iron Steel Res. Int.*, 23(2016), No. 10, p. 1071.
[42] L.Q. Guo, B.J. Yang, J.Y. He, and L.J. Qiao, Local electrical properties of thermally grown oxide films formed on duplex stainless steel surfaces, *Appl. Surf. Sci.*, 444(2018), p. 48.
[43] L.D. Chen, H. Tan, Z.Y. Wang, J. Li, and Y.M. Jiang, Influence of cooling rate on microstructure evolution and pitting corrosion resistance in the simulated heat-affected zone of 2304 duplex stainless steels, *Corros. Sci.*, 58(2012), p. 168.
[44] B. Deng, Z.Y. Wang, Y.M. Jiang, T. Sun, J.L. Xu, and J. Li, Effect of thermal cycles on the corrosion and mechanical properties of UNS S31803 duplex stainless steel, *Corros. Sci.*, 51(2009), No. 12, p. 2969.
[45] H. Tan, Z.Y. Wang, Y.M. Jiang, Y.Z. Yang, B. Deng, H.M. Song, and J. Li, Influence of welding thermal cycles on microstructure and pitting corrosion resistance of 2304 duplex stainless steels, *Corros. Sci.*, 55(2012), p. 368.
[46] H. Tan, Z.Y. Wang, Y.M. Jiang, D. Han, J.F. Hong, L.D. Chen, L.Z. Jiang, and J. Li, Annealing temperature effect on the pitting corrosion resistance of plasma arc welded joints of duplex stainless steel UNS S32304 in 1.0 M NaCl, *Corros. Sci.*, 53(2011), No. 6, p. 2191.
[47] Y.Z. Yang, Z.Y. Wang, H. Tan, J.F. Hong, Y.M. Jiang, L.Z. Jiang, and J. Li, Effect of a brief post-weld heat treatment on the microstructure evolution and pitting corrosion of laser beam welded UNS S31803 duplex stainless steel, *Corros. Sci.*, 65(2012), p. 472.
[48] L.W. Wang, H.Y. Tian, H. Gao, F.Z. Xie, K. Zhao, and Z.Y. Cui, Electrochemical and XPS analytical investigation of the accelerative effect of bicarbonate/carbonate ions on AISI 304 in alkaline environment, *Appl. Surf. Sci.*, 492(2019), p. 792.
[49] Z.Y. Cui, S.S. Chen, L.W. Wang, C. Man, Z.Y. Liu, J.S. Wu, X. Wang, S.G. Chen, and X.G. Li, Passivation behavior and surface chemistry of 2507 super duplex stainless steel in acidified artificial seawater containing thiosulfate, *J. Electrochem. Soc.*, 164(2017), No. 13, p. C856.
[50] A. Pardo, M.C. Merino, A.E. Coy, F. Viejo, R. Arrabal, and E. Matykina, Pitting corrosion behaviour of austenitic stainless steels—Combining effects of Mn and Mo additions, *Corros. Sci.*, 50(2008), No. 6, p. 1796.
[51] C.M. Abreu, M.J. Cristobal, R. Losada, X.R. Nóvoa, G. Pena, and M.C. Pérez, High frequency impedance spectroscopy study of passive films formed on AISI 316 stainless steel in alkaline medium, *J. Electroanal. Chem.*, 572(2004), No. 2, p. 335.
[52] K. Hashimoto, K. Asami, and K. Teramoto, An X-ray photoelectron spectroscopic study on the role of molybdenum in increasing the corrosion resistance of ferritic stainless steels in HC1, *Corros. Sci.*, 19(1979), No. 1, p. 3.